

Fully spin-polarized, valley-polarized and spin-valley-polarized electron beam splitters utilizing zero-line modes in a three-terminal device

Xiao-Long Lü(吕小龙), Jia-En Yang(杨加恩), and Hang Xie(谢航),

Citation: Chin. Phys. B, 2024, 33 (**6**): 068502. DOI: 10.1088/1674-1056/ad2609
Journal homepage: http://cpb.iphy.ac.cn; http://iopscience.iop.org/cpb

What follows is a list of articles you may be interested in

Valleytronic topological filters in silicene-like inner-edge systems

Hang Xie(谢航), Xiao-Long Lü(吕小龙), and Jia-En Yang(杨加恩)
Chin. Phys. B, 2024, 33 (**1**): 018502. DOI: 10.1088/1674-1056/ad0714

Temperature dependence of spin pumping in YIG/NiO_x/W multilayer

Lijun Ni(倪丽君), Wenqiang Wang(王文强), Lichuan Jin(金立川), Jiandong Ye(叶建东), Hehe Gong(巩贺贺), Xiang Zhan(战翔), Zhendong Chen(陈振东), Longlong Zhang(张龙龙), Xingze Dai(代兴泽), Yao Li(黎遥), Rong Zhang(张荣), Yi Yang(杨燚), Huaiwu Zhang(张怀武), Ronghua Liu(刘荣华), Lina Chen(陈丽娜), and Yongbing Xu(徐永兵)
Chin. Phys. B, 2022, 31 (**12**): 128504. DOI: 10.1088/1674-1056/ac6333

Optical nuclear spin polarization in quantum dots

Ai-Xian Li(李爱仙), Su-Qing Duan(段素青), Wei Zhang(张伟)
Chin. Phys. B, 2016, 25 (**10**): 108506. DOI: 10.1088/1674-1056/25/10/108506

Improved double-gate armchair silicene nanoribbon field-effect-transistor at large transport bandgap

Mohsen Mahmoudi, Zahra Ahangari, Morteza Fathipour
Chin. Phys. B, 2016, 25 (**1**): 018501. DOI: 10.1088/1674-1056/25/1/018501

Current-induced pseudospin polarization in silicene

Wang Lei (王磊), Zhu Guo-Bao (朱国宝)
Chin. Phys. B, 2014, 23 (**9**): 098503. DOI: 10.1088/1674-1056/23/9/098503

Fully spin-polarized, valley-polarized and spin-valley-polarized electron beam splitters utilizing zero-line modes in a three-terminal device

Xiao-Long Lü(吕小龙)[1], Jia-En Yang(杨加恩)[2,†], and Hang Xie(谢航)[2,3,‡]

[1] *College of Science, Guangxi University of Science and Technology, Liuzhou* 545006, *China*
[2] *College of Physics, Chongqing University, Chongqing* 401331, *China*
[3] *Chongqing Key Laboratory for Strongly-Coupled Physics, Chongqing University, Chongqing* 401331, *China*

(Received 30 August 2023; revised manuscript received 29 January 2024; accepted manuscript online 5 February 2024)

Topological zero-line modes (ZLMs) with spin and valley degrees of freedom give rise to spin, valley and spin-valley transport, which support a platform for exploring quantum transport physics and potential applications in spintronic/valleytronic devices. In this work, we investigate the beam-splitting behaviors of the charge current due to the ZLMs in a three-terminal system. We show that with certain combinations of ZLMs, the incident charge current along the interface between different topological phases can be divided into different polarized currents with unit transmittance in two outgoing terminals. As a result, fully spin-polarized, valley-polarized and spin-valley-polarized electron beam splitters are generated. The mechanism of these splitters is attributed to the cooperative effects of the distribution of the ZLMs and the intervalley and intravalley scatterings that are modulated by the wave-vector mismatch and group velocity mismatch. Interestingly, half-quantized transmittance of these scatterings is found in a fully spin-valley-polarized electron beam splitter. Furthermore, the results indicate that these splitters can be applicable to graphene, silicene, germanene and stanene due to their robustness against the spin–orbit coupling. Our findings offer a new way to understand the transport mechanism and investigate the promising applications of ZLMs.

Keywords: topological zero-line modes, spin polarization, valley polarization, quantum transport

PACS: 85.75.–d, 05.60.Gg, 73.20.At, 73.63.–b **DOI:** 10.1088/1674-1056/ad2609

1. Introduction

Due to the regulated linear Dirac dispersion,[1–3] graphene-like materials with a honeycomb lattice structure, such as graphene itself,[4] silicene,[5,6] germanene[7,8] and stanene,[9,10] are ideal platforms for investigating fundamental quantum transport physics and have a wide range of applications in device design. It has been found that graphene-like materials can exhibit abundant topological phases under different external fields applied to the whole system,[11–15] and the side potential applied to the boundary of the system is also crucial for generating and manipulating topological phases and corresponding edge states.[16,17] In particular, a large number of zero-line modes (ZLMs)[18–20] that can arise from the interface separating different topological phases have been found in addition to outer edge states[11,21–23] induced at the interface between topological phases and the topologically trivial vacuum. In particular, ZLMs are related not only to the Chern numbers but also to the valley Chern numbers, which are also known as kink states and inner edge states, respectively. Different types of ZLMs are dependent on different combinations of topological phases between the interfaces, which can be generated by spatially varying external fields.[24–27]

ZLMs containing charge, spin and valley degrees of freedom can simultaneously give rise to abundant charge, spin and valley transport phenomena, which have promising applications in multifunctional devices.[26,28,29] Similar to spintronics, the central issues of valleytronics and spin-valleytronics are the generation and manipulation of valley-polarized and spin-valley-polarized currents, respectively. Recently, ZLMs have been extensively investigated in quantum transport. Using a spatially varying electric field in two-terminal zigzag graphene-like materials, valley-polarized and spin-valley-polarized currents can be obtained due to the valley-momentum and spin-valley-momentum locked conducting channels, which can be regarded as valley and spin-valley filters.[30,31] Besides, double-output and single-output spin-valley filters can be generated by manipulating the spin-valley-polarized current in a three-terminal device.[32] The conductance of the ZLMs is also robust against different kinds of long-range and short-range disorders.[24,33] In particular, the ZLMs at an intersection in four-terminal systems can be used to design charge, spin-polarized and valley-polarized electron beam splitters.[34–39]

The transport properties of ZLMs and their application have been extensively investigated. But there are still some interesting and important points that need to be explored in more depth. Firstly, the cooperative effect of the distribution of ZLMs and the intervalley and intravalley scatterings of ZLMs in multi-terminal devices is rarely considered; these

†Corresponding author. E-mail: yangjiaen309@163.com
‡Corresponding author. E-mail: xiehangphy@cqu.edu.cn

© 2024 Chinese Physical Society and IOP Publishing Ltd

play an important role in generating different polarized currents and are a basis for exploring other interesting transport phenomena. Secondly, it is difficult to simultaneously propose fully spin-polarized, valley-polarized and spin-valley-polarized electron beam splitters[34–39] as multifunctional couplers utilizing ZLMs. Lastly, it is not known whether a multifunctional coupler is suitable for graphene-like materials with different spin–orbit couplings.

In this work, we construct a three-terminal device (shown in Fig. 1) in which the conductor and incident lead (lead 1) are fixed at the same ZLM with two valleys, and the transmitted leads (leads 2 and 3) are fixed at different ZLMs with a single valley. It is demonstrated that the incident current composed of two valley currents can be divided into completely different polarized currents, which is attributed to the distributions and valley scatterings of the ZLMs. As a result, a three-terminal device can be regarded as a multifunctional coupler incorporating fully spin-polarized, valley-polarized and spin-valley-polarized electron beam splitters. Compared with a four-terminal system, our proposed device utilizing different ZLMs is versatile. In particular, these splitters are robust against spin–orbit coupling (SOC), which enables the results to be applicable to graphene, silicene, germanene and stanene.

2. Model and methods

By utilizing different ZLMs, we construct a three-terminal device composed of a conductor and three leads to generate three types of polarized current, such as the valley-polarized, spin-polarized and spin-valley-polarized currents in Fig. 1(a). The ZLMs are distributed at the interfaces separating different topological phases in regions I and II in three leads and the conductor. The charge current is assumed to propagate from lead 1 (incident lead) and transmit into leads 2 and 3 (transmitted leads), and the incident lead and conductor are identical; the band structures and corresponding ZLMs are shown in Figs. 1(b) and 1(c). The tight-binding Hamiltonian of the three-terminal device made of zigzag hybrid graphene-like nanoribbons is written as[22,40]

$$\begin{aligned} H = & -t\sum_{\langle i,j\rangle\alpha} c^{\dagger}_{i\alpha}c_{j\alpha} + \mathrm{i}\frac{\lambda_{\mathrm{so}}}{3\sqrt{3}}\sum_{\langle\langle i,j\rangle\rangle\alpha\beta} \upsilon_{ij}c^{\dagger}_{i\alpha}\sigma^{Z}_{\alpha\beta}c_{j\beta} \\ & + \mathrm{i}\frac{\lambda_{\Omega}}{3\sqrt{3}}\sum_{\langle\langle i,j\rangle\rangle\alpha} \upsilon_{ij}c^{\dagger}_{i\alpha}c_{j\alpha} \\ & + \lambda_{\mathrm{AF}}\sum_{i\alpha\beta}\mu_i c^{\dagger}_{i\alpha}\sigma^{Z}_{\alpha\beta}c_{i\beta} + \lambda_{\mathrm{E}}\sum_{i\alpha}\mu_i c^{\dagger}_{i\alpha}c_{i\alpha}, \end{aligned} \tag{1}$$

where the operator $c^{\dagger}_{i\alpha}$ ($c_{i\alpha}$) creates (annihilates) an electron at site i with spin α, and $\sigma^{Z}_{\alpha\beta}$ is the Z-component Pauli matrix with spin indices α and β. $\langle i,j\rangle$ and $\langle\langle i,j\rangle\rangle$ denote the sum over nearest-neighbor and next-nearest-neighbor hopping sites, respectively. The first term denotes nearest-neighbor hopping with $t = 1$ eV being a unit of other fields. The second term is intrinsic SOC with strength λ_{so}, and $\upsilon_{ij} = +1$ (-1) as next-nearest-neighbor hopping is anticlockwise (clockwise) with respect to the positive z-axis. The third term denotes the Haldane model induced by off-resonant circularly polarized (ORCP) light with intensity λ_{Ω}, where the $(\pm)$ sign of λ_{Ω} denotes right and left polarized directions, respectively.[41–43] The intensity of the ORCP light is expressed as $\lambda_{\Omega} = 9t^2J_1^2(\Lambda)/(\hbar\omega)$,[44] where $\Lambda = Aea/\hbar$ is dimensionless light intensity with light amplitude A and J_1 is a first-order Bessel function. The off-resonance condition can be satisfied when $\hbar\omega \gg t$, and the lowest frequency is determined by the bandwidth $\hbar\omega = 3t$,[1,45] which is about 1.69×10^{15} Hz for graphene. In addition, Λ is generally less than 1. If the lowest frequency and $\Lambda = 0.5$ are accepted, the intensity is translated as $\lambda_{\Omega} = 0.176t$. For graphene, silicene, germanene and stanene vertically irradiated by off-resonant circularly polarized light, the intensity could exceed 0.2 eV. Without changing the off-resonant condition $\hbar\omega = 3t$, the intensity λ_{Ω} can be modulated by the dimensionless light intensity z. The fourth term is the antiferromagnetic exchange field λ_{AF} with $\mu_i = 1$ for the sublattice A and $\mu_i = -1$ for the sublattice B, which can be induced by ferromagnetic substrates.[13,46,47] The last term is the staggered potential with strength λ_{E}, which can be easily induced for buckled honeycomb structures by the gate voltage. But for graphene, with a planar structure, this term can be realized by putting the graphene on the hexagonal boron nitride (hBN).[48,49]

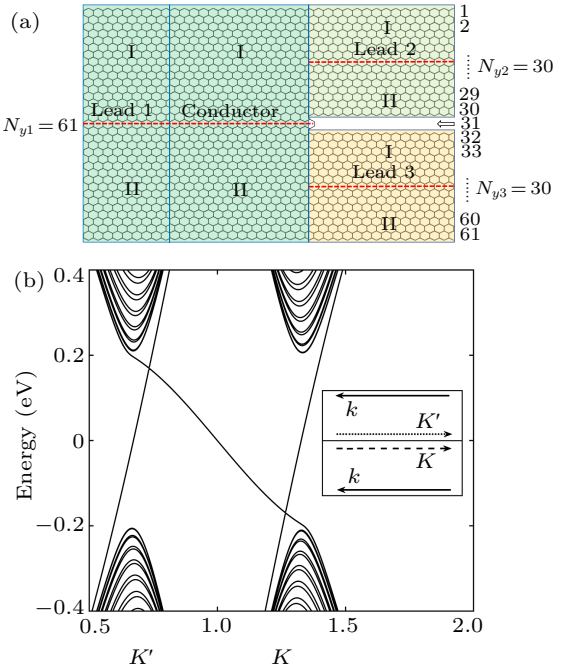


Fig. 1. (a) Schematic diagram of a three-terminal device including four parts: lead 1, conductor, lead 2 and lead 3. Each part is made of a hybrid zigzag graphene-like nanoribbon where the red dotted lines denote the interfaces between regions I and II, and lead 1 and the conductor are identical. (b) The band structure and corresponding ZLM for lead 1 and the conductor. The corresponding parameters are set as $-\lambda^{\mathrm{I}}_{\Omega} = \lambda^{\mathrm{II}}_{\Omega} = 0.2t$, $\lambda^{\mathrm{I}}_{\mathrm{AF}} = \lambda^{\mathrm{II}}_{\mathrm{AF}} = 0$, $\lambda^{\mathrm{I}}_{\mathrm{E}} = \lambda^{\mathrm{II}}_{\mathrm{E}} = 0$, $\lambda_{\mathrm{so}} = 0$. The fixed values of the subunit along the armchair boundary are set as $N_{y1} = 61$, $N_{y2} = 30$, $N_{y1} = 30$, and each subunit contains four atoms.

To character the ZLMs mainly distributed at the interface between regions I and II with different topological phases, one can use the difference in the spin- and valley-dependent Chern numbers $\Delta C_{\eta s} = C^{\rm II}_{\eta s} - C^{\rm I}_{\eta s}$, where the subscript $\eta = \pm 1$ denotes the valleys K and K' and $s = \pm 1$ denotes the spin-up and spin-down modes. $C^{\rm I}_{\eta s}$ and $C^{\rm II}_{\eta s}$ characterize the topological phases in regions I and II, and the type and sign of $\Delta C_{\eta s}$ correspond to different spin-valley ZLMs and their propagation direction, respectively. For instance, a positive (negative) sign of $\Delta C_{\eta s}$ denotes the right (left) propagation direction. Furthermore, the Chern numbers $C_{\eta s}$ can be calculated by $C_{\eta s} = \frac{\eta}{2}{\rm sgn}(\Delta_{\eta s})$, where the Dirac mass terms can be obtained as $\Delta_{\eta s} = \eta s\lambda_{\rm so} + \eta\lambda_\Omega + s\lambda_{\rm AF} + \lambda_{\rm E}$ based on the low-energy Hamiltonian of Eq. (1) in momentum space. According to the formula for $\Delta C_{\eta s}$, some fascinating ZLMs can be found.

To investigate the mechanism of the intervalley scattering, intravalley scattering and application of ZLMs, we use the wave-function matching technique.[50,51] Following these works, one can regard the effect of the leads on the conductor as the self-energy, and the transmission coefficient is calculated as

$$T^{ab}_{mn} = \left| t^{ab}_{mn} \right|^2, \tag{2}$$

where t^{ab}_{mn} denotes the transmission amplitude from the incoming mode n in the incident lead b to an outgoing mode m in the transmitted lead a. Based on the Schrödinger equation and wave-function matching technique, the local bond current propagating from atoms i to j with the incoming mode m in lead 1 can be obtained as

$$J^m_{ji} = \frac{\rm i}{\hbar}\left[H_{ji}(\psi^m_{D,j})^\dagger \psi^m_{D,i} - H_{ij}(\psi^m_{D,i})^\dagger \psi^m_{D,j}\right], \tag{3}$$

where H_{ji} and ψ^m_D are the Hamiltonian element and the wave function with the incoming mode m of the scattering region, respectively. In addition, the scattering region not only contains the conductor but also the leftmost unit cells in leads 2 and 3. Details of the derivation of Eq. (3) were introduced in Ref. [40]. It is noted that the transport processes can be visually observed by the local bond current, which plays an important role in understanding the transport mechanism.

3. Results and discussion

Before discussing the following results, we introduce the fixed parameters of the proposed three-terminal device. The widths along the armchair boundary of three leads are set as $N_{y1} = 61$, $N_{y2} = N_{y3} = 30$, respectively, and each subunit contains four atoms. The structure in Fig. 1(a) is symmetrical with respect to the red dotted line in lead 1 and the conductor, and the distance between leads 2 and 3 is set as four atoms. These designs aim to decrease the reflection for a perfect transport effect.[32]

3.1. ZLMs with a single valley

Spin-degeneracy and spin-polarized ZLMs with a different single valley can be generated under different external fields in regions I and II. Figure 2(a) shows that the ZLM with valley K' propagates to the right, while the outer edge state propagates to the left, and can be generated by the ORCP light in region II and the staggered potential in region I.

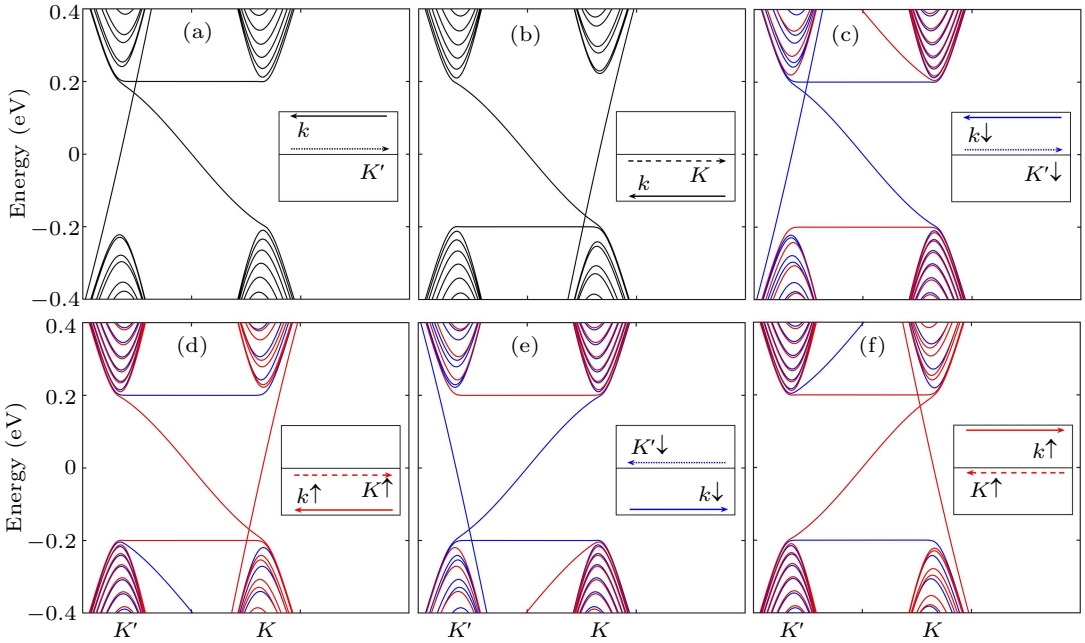


Fig. 2. The band structures and corresponding ZLMs with a single valley under different external fields of (a) $-\lambda^{\rm I}_\Omega = -\lambda^{\rm II}_{\rm E} = 0.2t$, (b) $\lambda^{\rm II}_\Omega = -\lambda^{\rm I}_{\rm E} = 0.2t$, (c) $-\lambda^{\rm I}_\Omega = \lambda^{\rm I}_{\rm E} = \lambda^{\rm I}_{\rm AF} = \lambda^{\rm II}_{\rm AF} = 0.2t$, (d) $\lambda^{\rm II}_\Omega = \lambda^{\rm II}_{\rm E} = -\lambda^{\rm I}_{\rm AF} = -\lambda^{\rm II}_{\rm AF} = 0.2t$, (e) $-\lambda^{\rm II}_\Omega = \lambda^{\rm II}_{\rm E} = \lambda^{\rm II}_{\rm AF} = \lambda^{\rm I}_{\rm AF} = 0.2t$ and (f) $\lambda^{\rm I}_\Omega = \lambda^{\rm I}_{\rm E} = -\lambda^{\rm I}_{\rm AF} = -\lambda^{\rm II}_{\rm AF} = 0.2t$. The insets within (a)–(f) show the edge state distributions, and black, blue and red denote the spin-degeneracy, spin-down and spin-up modes, respectively.

The corresponding band structure is shown in Fig. 2(a), which can be used to calculate the distribution of the edge states. Similarly, one can also obtain a ZLM with valley K flowing to the right in the inset in Fig. 2(b), with the corresponding band structure in the main figure. In particular, the combination of an antiferromagnetic exchange field, the ORCP light and a staggered potential can break the spin-degeneracy mode while maintaining the valley-polarized ZLM. As a consequence, abundant spin-valley-polarized ZLMs are generated in the insets in Figs. 2(c)–2(f), with the corresponding band structures being shown in the main figures. Note that the ZLMs exist in the large bulk gap similar to the large-gap quantum spin Hall effect.[52] We choose the one in Fig. 2(c) as an example to illustrate the formation of ZLMs by the spin- and valley-dependent Chern number $\Delta C_{\eta s}$. The Chern numbers in regions I and II are obtained as $C_{\eta s}^{\mathrm{I/II}} = \frac{\eta}{2}\mathrm{sgn}\left(\Delta_{\eta s}^{\mathrm{I/II}}\right)$, where the mass Dirac terms are expressed as $\Delta_{\eta s}^{\mathrm{I}} = \eta\lambda_{\Omega}^{\mathrm{I}} + \lambda_{\mathrm{E}}^{\mathrm{I}} + s\lambda_{\mathrm{AF}}^{\mathrm{I}}$ and $\Delta_{\eta s}^{\mathrm{II}} = s\lambda_{\mathrm{AF}}^{\mathrm{II}}$, respectively. Then, the spin- and valley-dependent Chern numbers are calculated as $\left(\Delta C_{K\uparrow}, \Delta C_{K'\uparrow}, \Delta C_{K\downarrow}, \Delta C_{K'\downarrow}\right) = (0,0,0,1)$, indicating that only the ZLM with a spin-down mode and valley K' exists and propagates to the right. These different ZLMs all support unidirectional conductance, in which time-reversal symmetry is broken.

3.2. A fully valley-polarized electron beam splitter

By utilizing the ZLMs from Fig. 2, we construct a three-terminal device in Fig. 3(a) to generate a fully valley-polarized splitter. The figure shows that there are two propagating channels in the left region (containing lead 1 and the conductor) and one propagating channel in each of leads 2 and 3. We expect that the incident currents flowing along the interface in the left region can be divided into two transmitted currents along the interfaces in leads 2 and 3 with unit transmittance. In Figs. 3(b1), 3(b2) and 3(c1), the transmission and local bond currents confirm this transport phenomenon. By considering valleys K and K' in Fig. 3(b), one can find that the transmissions $T_{K'K}^{21}$ and $T_{KK'}^{31}$ of the intervalley scattering are significantly smaller than the transmissions $T_{K'K'}^{21}$ and T_{KK}^{31} of the intravalley scattering. Due to the wave-vector mismatch (or the large distance between valleys K and K'), most of the incident current within valley K' transmits into the propagating channel within valley K' in lead 2, and a small amount of current transmits into lead 3 with intervalley scattering from K' to K, as shown in Fig. 3(c2). Similarly, the transport phenomena of the incident current within valley K are consistent with that in Fig. 3(b2), as shown in Fig. 3(b3). The unit transmittance in leads 2 and 3 originates from the contribution of intervalley and intravalley scattering. As a consequence, the charge current propagating along the interface in the left region is split into two fully valley-polarized currents in leads 2 and 3.

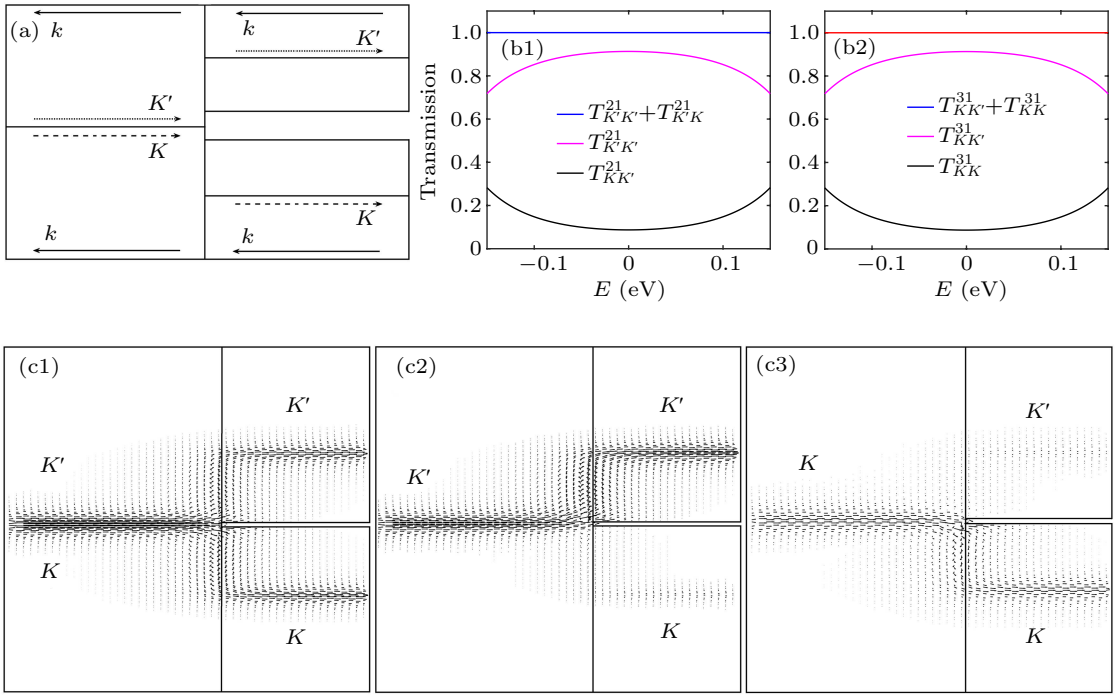


Fig. 3. (a) Schematic diagram of a three-terminal device, where each part is under a different ZLM from Fig. 2. (b) The corresponding transmissions from lead 1 to leads 2 and 3, respectively. (c) Local bond currents with different incoming modes (K', K, K' and K modes) at $E = -0.05$ eV.

3.3. A fully spin-valley-polarized electron beam splitter

Different spin-valley-polarized currents can be generated from the partition of the charge current in a three-terminal device, and half-quantized transmittance of the intervalley and intravalley scatterings is found. In Fig. 4(a), we can see that there exist spin-up and spin-down transmitted channels with

different valleys in leads 2 and 3, respectively. Meanwhile, two outer edge states support the reflected channels in the left regions. Based on these distributions of the propagating channel, we expect some fascinating transport phenomena. Figure 4(b) shows that the total transmittance originating from the intervalley and intravalley scatterings is 1. The transport mechanisms can be explained by the local bond currents in Fig. 4(c). This figure shows that the incident charge current is split into two beams of fully spin-polarized current. For the spin-down mode, part of the current flows upward and then turns right to the transmitted channel with unit transmittance and without flowing to the upper reflected channel due to the characteristic of nearest path selection; the rest of the current flows downward and then turns back to the lower reflected channel. The contribution of total transmission of the spin-down mode (the blue line in Fig. 4(b1)) originates from the half-quantized transmittance of the intervalley and intravalley scatterings. In particular, one can see that when the added group velocity mismatch induced by the SOC disappears, the intervalley and intravalley scatterings retain a half-integer, which is explained in detail in Fig. 8. Likewise, for the spin-up mode, the propagating phenomena and mechanism are identical to the spin-down case; the transmission and local bond current are shown in Figs. 4(b2) and 4(c2).

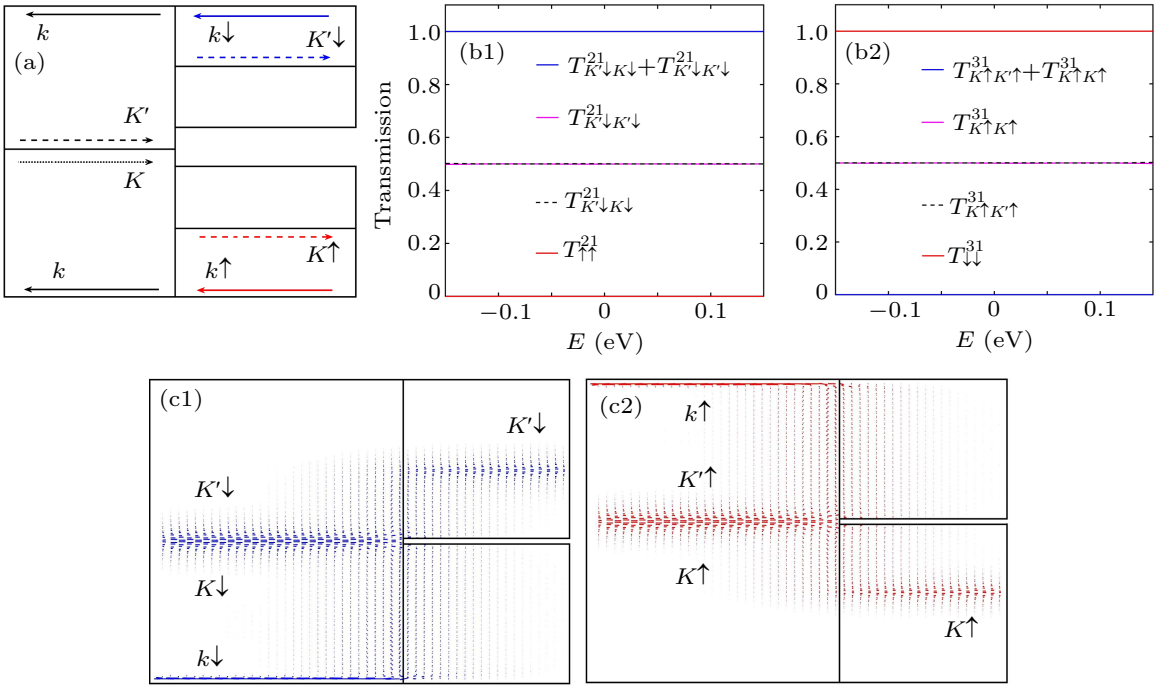


Fig. 4. (a) Schematic diagram of a three-terminal device containing different ZLMs that are taken from Fig. 2. (b) The transmissions from lead 1 to leads 2 and 3. (c) The corresponding local bond currents with incoming modes K', K at $E = -0.05$ eV.

3.4. A fully spin-polarized electron beam splitter

This splitter, where the incident charge current propagating along the interface in lead 1 is divided into different spin-polarized currents in leads 2 and 3, can be generated in a specific system shown in Fig. 5(a): this shows the lower spin-down transmitted channel in lead 2 and the upper spin-up transmitted channel in lead 3, while two outer reflected channels exist in the left region. These ZLM distributions support a variety of possible propagating paths. In Fig. 5(b1), the total transmittance of $T^{21}_{k\downarrow K'\downarrow}+T^{21}_{k\downarrow K\downarrow}$ (blue line) is 1, which indicates that one of two beams of the spin-down current splits from the charge current in Fig. 5(a), and then transmits into the spin-down channel in the lower boundary in lead 2. The corresponding local bond current in Fig. 5(c1) exhibits this transport phenomenon, and also shows that the other beam of spin-down current flows downward and then turns back to the lower reflected channel. In particular, the transmittance $T^{21}_{k\downarrow K\downarrow}$ from the valley K to k is larger than the transmittance $T^{21}_{k\downarrow K'\downarrow}$, which is attributed to the wave-vector mismatch. From the band structures of lead 2 and the left region shown in Figs. 2(e) and 1(b), respectively, one can see that the wave-vector mismatch between k and K gradually decreases with increasing incident energy E, while the tendency for valley K' is the opposite, which leads to the increasing and decreasing tendencies of transmissions $T^{21}_{k\downarrow K\downarrow}$ and $T^{21}_{k\downarrow K'\downarrow}$, respectively. Actually, the transport phenomena and mechanism of the incident spin-up current that is split from the charge current in the left region are identical to those of the spin-down current, and the corresponding transmission and local bond current are shown in Figs. 5(b2) and 5(c2).

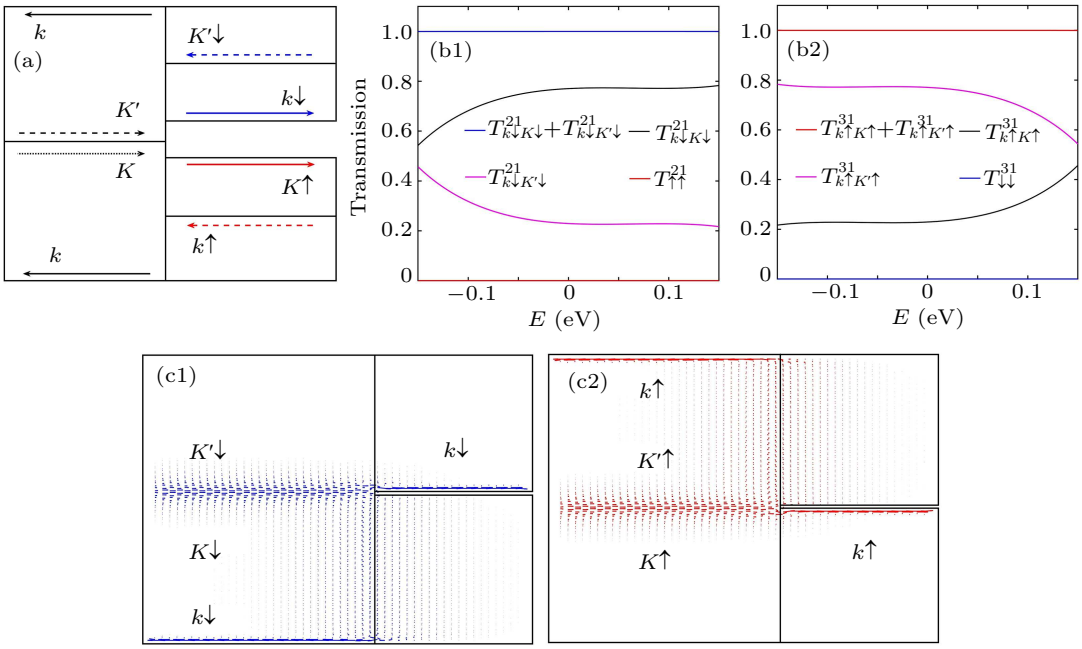


Fig. 5. (a) Schematic diagram of a three-terminal device with different ZLMs taken from Fig. 2. (b) The transmissions from lead 1 to leads 2 and 3. (c) The corresponding local bond currents with incoming modes K', K at $E = -0.05$ eV.

3.5. The effect of SOC on splitters

Following the values of SOC in silicene, germanene and stanene, the region of SOC for the results below is set as $\lambda_{so} \leq 0.1t$. In the presence of SOC, the fully valley-polarized, spin-polarized and spin-valley-polarized electron beam splitters are not destroyed and the total transmittance is still constant, as discussed in Fig. 6. Here, we choose the fully spin-valley-polarized electron beam splitter as an example for discussing the effect of SOC. In Fig. 6(a), the transmissions are reproduced from Fig. 4(b) to highlight the effect of SOC. Figures 6(b)–6(d) show that the half-quantized transmissions are obviously broken with increase in the SOC, where the transmittance of the intervalley (intravalley) scattering increases (decreases). In particular, the total transmission remains unchanged (the blue and red) with decrease in the energy region, which indicates that the fully spin-valley-polarized electron beam splitter has not been destroyed. Therefore, these designed splitters are applicable to graphene, silicene, germanene and stanene.

Here, we explain how the splitter remains steady and the half-quantized transmissions of the intervalley and intravalley scatterings are broken in the presence of SOC. In Figs. 7(a)–7(c), one can see that with increasing SOC strength two bands (red) near the valleys for the ZLMs in the left region remain steady while their bulk gap decreases. Actually, ZLMs in leads 2 and 3 also remain steady (but are not shown here because the region of the SOC being discussed is independent of changes in the spin- and valley-dependent Chern numbers $\Delta C_{\eta s}$). Therefore, the constant distribution of the ZLMs with decrease in the energy region in the three-terminal device corresponds to a steady fully spin-valley-polarized splitter with a smaller energy region, as shown in Fig. 6. The other splitters that are also steady are not shown here.

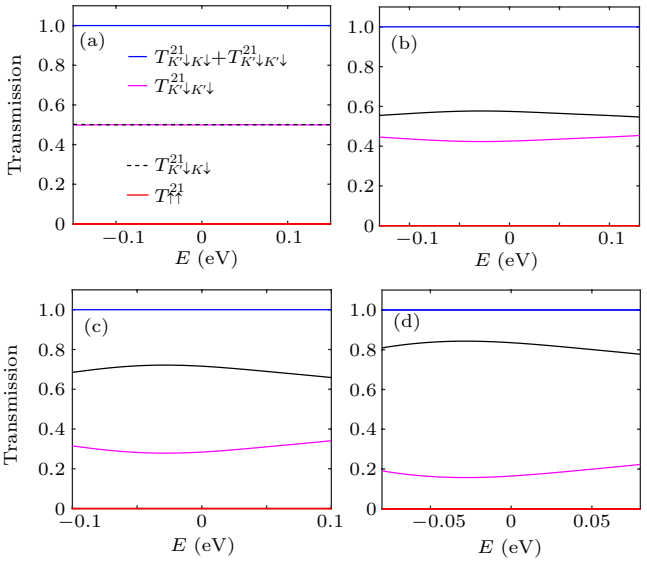


Fig. 6. The transmission from lead 1 to lead 2 is reproduced in (a) from Fig. 4(b) to highlight the effect of SOC: (b) $\lambda_{so} = 0.02t$, (c) $\lambda_{so} = 0.06t$, (d) $\lambda_{so} = 0.1t$. SOC is applied to the whole three-terminal device. The other trends of transmission from lead 1 to lead 3 are almost identical and are not shown here.

For the broken transmissions in Fig. 7(a) one can also find that compared with the black band structure without SOC, the group velocity mismatch (the slope of the bands) between the bands for lower edge states and the bands for the ZLMs with K' obviously decrease, and most of the current within the valley K' flows back to the lower boundary shown in Fig. 8(b). This is a reason why the transmittance of the intravalley scattering decreases with the increase in SOC shown in Fig. 7. The total reflection from valleys K' and K remains as 1, which

causes a small amount of the current within valley K to be reflected along the lower boundary in the left region. As a result, most of the current within valley K transmits into lead 2 along the interface, as shown in Fig. 8(b). The total transmittance of the intervalley and intravalley scattering is still 1; the corresponding local bond current is shown in Fig. 8(c). Figure 8(d) shows that the total charge current can be divided into two beams of spin-polarized current with different spin modes, and then the current with a spin-up (spin-down) mode is divided again into the interface in leads 3 (2) and the outer (lower) boundary in the left region. As a consequence, a fully spin-valley-polarized splitter is generated where the different spin-valley-polarized currents are split into different leads. Actually, these results also show that the reason why the half-integer is broken is that an additional group velocity mismatch is induced by the SOC compared with the initial group velocity mismatch without SOC.

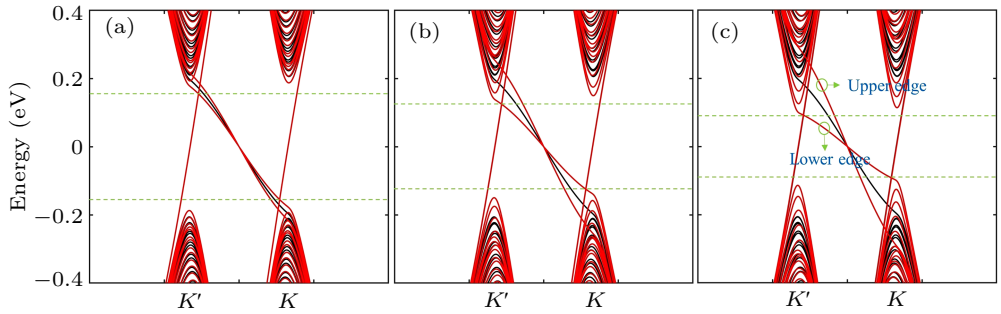


Fig. 7. Red denotes the band structure in the left region of the case in Fig. 4(a) with SOC of (a) $\lambda_{so} = 0.02t$, (b) $\lambda_{so} = 0.06t$ and (c) $\lambda_{so} = 0.1t$. Black denotes the case without SOC, and the green dashed box denotes the gap for inner and outer edge states.

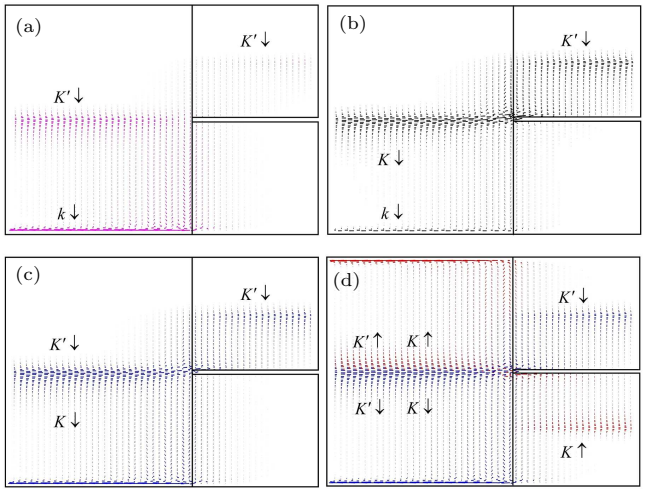


Fig. 8. The local bond currents at $E = -0.05$ eV correspond to the case in Fig. 4(a) with $\lambda_{\Omega} = 0.1t$. Panels (a) and (b) correspond to the intravalley and intervalley scattering of the spin-down mode from lead 1 to lead 2, respectively. (c) The sum of cases in (a) and (b). (d) The sum of local bond currents of both the spin-up and spin-down modes from lead 1 to leads 2 and 3.

4. Conclusion

We have investigated the transport mechanisms and applications of ZLMs in a three-terminal device. These results show that the incoming charge current flowing along the interface in the left region can be divided into different polarized currents in two transmitted terminals, such as fully spin-polarized, valley-polarized and spin-valley-polarized currents with different distributions of ZLMs. In addition, the transport phenomena are also dependent on the intervalley and intravalley scatterings modulated by the wave-vector mismatch and group velocity mismatch, which enable the three-terminal device to operate as different electron beam splitters. In particular, the half-quantized transmissions of these valley scatterings were discovered. These splitters are barely influenced by SOC, which indicates that all the properties concerned can be applicable to graphene, silicene, germanene and stanene.

Acknowledgements

Project supported by the National Natural Science Foundation of China (Grant Nos. 12304058, 12204073, and 12147102), Guangxi Science and Technology Base and Talent Project (Grant No. 2022AC21077), Natural Science Foundation of Guangxi Province (Grant No. 2024GXNSFBA010229), and Foundation of Guangxi University of Science and Technology (Grant No. 21Z52).

References

[1] Ezawa M 2013 *Phys. Rev. Lett.* **110** 026603
[2] Pan H, Li Z S, Liu C C, Zhu G B, Qiao Z H and Yao Y G 2014 *Phys. Rev. Lett.* **112** 106802
[3] Zhao X Y, Wang Z T, Chen J P and Wang B 2023 *J. Phys. Condens. Mat.* **35** 095401
[4] Novoselov K S, Geim A K, Morozov S V, Jiang D, Zhang Y, Dubonos S V, Grigorieva I V and Firsov A A 2004 *Science* **306** 666
[5] Fleurence A, Friedlein R, Ozaki T, Kawai H, Wang Y and Yamada-Takamura Y 2012 *Phys. Rev. Lett.* **108** 245501
[6] Vogt P, De Padova P, Quaresima C, Avila J, Frantzeskakis E, Asensio M C, Resta A, Ealet B and Le Lay G 2012 *Phys. Rev. Lett.* **108** 155501
[7] Bianco E, Butler S, Jiang S S, Restrepo O D, Windl W and Goldberger J E 2013 *ACS Nano* **7** 4414
[8] Davila M E, Xian L, Cahangirov S, Rubio A and Le Lay G 2014 *New J. Phys.* **16** 095002
[9] Xu Y, Yan B H, Zhang H J, Wang J, Xu G, Tang P Z, Duan W H and Zhang S C 2013 *Phys. Rev. Lett.* **111** 136804
[10] Zhu F F, Chen W J, Xu Y, Gao C L, Guan D D, Liu C H, Qian D, Zhang S C and Jia J F 2015 *Nat. Mater.* **14** 1020
[11] Ezawa M 2015 *J. Phys. Soc. Jpn.* **84** 121003

[12] Frank T, Hogl P, Gmitra M, Kochan D and Fabian J 2018 *Phys. Rev. Lett.* **120** 156402
[13] Hogl P, Frank T, Zollner K, Kochan D, Gmitra M and Fabian J 2020 *Phys. Rev. Lett.* **124** 136403
[14] Xu Y F, Ma J S and Jin G J 2021 *Phys. Rev. B* **104** 045416
[15] Zhuang Y C and Sun Q F 2022 *Phys. Rev. B* **106** 165417
[16] Lu W T, Sun Q F, Li Y F and Tian H Y 2021 *Phys. Rev. B* **104** 195419
[17] Yang J E, Lü X L and Xie H 2023 *Commun. Phys.* **6** 62
[18] Han Y L, Pan S Y and Qiao Z H 2023 *Phys. Rev. B* **108** 115302
[19] Liang W H, Hou T, Zeng J J, Liu Z, Han Y L and Qiao Z H 2023 *Phys. Rev. B* **107** 075303
[20] Ren Y F, Zeng J J, Wang K, Xu F M and Qiao Z H 2017 *Phys. Rev. B* **96** 155445
[21] Liu D P, Yu Z M and Liu Y L 2016 *Phys. Rev. B* **94** 155112
[22] Xu Y F and Jin G J 2017 *Phys. Rev. B* **95** 155425
[23] Zhang C X, Lu X L and Xie H 2020 *J. Phys. D* **53** 195302
[24] Han Y L, You S Y and Qiao Z H 2022 *Phys. Rev. B* **105** 155301
[25] Rzeszotarski B, Mrenca-Kolasinska A and Szafran B 2020 *Phys. Rev. B* **101** 115308
[26] Wang Z B, Cheng S G, Liu X and Jiang H 2021 *Nanotechnology* **32** 402001
[27] You S Y, Hou T, Li Z T and Qiao Z H 2022 *Phys. Rev. B* **106** L161413
[28] Martin I, Blanter Y M and Morpurgo A F 2008 *Phys. Rev. Lett.* **100** 036804
[29] Schaibley J R, Yu H Y, Clark G, Rivera P, Ross J S, Seyler K L, Yao W and Xu X D 2016 *Nat. Rev. Mater.* **1** 16055
[30] Jana K and Muralidharan B 2022 *Npj 2D Mater. Appl.* **6** 19
[31] Sun Y M, Zhao H, Yu Z M and Pan H 2019 *J. Appl. Phys.* **125** 123904
[32] Yang J E, Lu X L, Zhang C X and Xie H 2020 *New. J. Phys.* **22** 053034
[33] Zhou T, Cheng S G, Schleenvoigt M, Schuffelgen P, Jiang H, Yang Z Q and Zutic I 2021 *Phys. Rev. Lett.* **127** 116402
[34] Hsieh S H and Chu C S 2016 *Appl. Phys. Lett.* **108** 033113
[35] Qiao Z H, Jung J, Lin C W, Ren Y F, MacDonald A H and Niu Q 2014 *Phys. Rev. Lett.* **112** 206601
[36] Sanz S, Brandimarte P, Giedke G, Sánchez-Portal D and Frederiksen T 2020 *Phys. Rev. B* **102** 035436
[37] Sanz S, Papior N, Giedke G, Sánchez-Portal D, Brandbyge M and Frederiksen T 2022 *Phys. Rev. Lett.* **129** 037701
[38] Zhai F, Ma Y L and Chang K 2011 *New J. Phys.* **13** 083029
[39] Zhu W W, Long Y, Chen H and Ren J 2019 *Phys. Rev. B* **99** 115410
[40] Lü X L, Xie H, Yang J E, Li R X, Du L, Chen H J and Zhang H S 2023 *New J. Phys.* **25** 023016
[41] Lü X L and Xie H 2020 *New J. Phys.* **22** 073003
[42] Lü X L and Xie H 2022 *Commun. Theor. Phys.* **74** 035702
[43] Mohan P, Saxena R, Kundu A and Rao S 2016 *Phys. Rev. B* **94** 235419
[44] Eckardt A and Anisimovas E 2015 *New J. Phys.* **17** 093039
[45] Zheng J, Xiang Y, Li C L, Yuan R Y, Chi F and Guo Y 2020 *Phys. Rev. Appl.* **14** 034027
[46] Yokoyama T 2013 *Phys. Rev. B* **87** 241409
[47] Zollner K, Gmitra M, Frank T and Fabian J 2016 *Phys. Rev. B* **94** 155441
[48] Dean C R, Young A F, Meric I, Lee C, Wang L, Sorgenfrei S, Watanabe K, Taniguchi T, Kim P, Shepard K L and Hone J 2010 *Nat. Nanotechnol.* **5** 722
[49] Dyrdal A and Barnas J 2017 *2D Mater.* **4** 034003
[50] Ando T 1991 *Phys. Rev. B* **44** 8017
[51] Khomyakov P A, Brocks G, Karpan V, Zwierzycki M and Kelly P J 2005 *Phys. Rev. B* **72** 035450
[52] Zhang H S, Wang Y Y, Yang W J, Zhang J J, Xu X H and Liu F 2021 *Nano Lett.* **21** 5823